PAPER • **OPEN ACCESS**

Plasma performance and operational space with an RMP-ELM suppressed edge

To cite this article: C. Paz-Soldan *et al* 2024 *Nucl. Fusion* **64** 096004

OPEN ACCESS
IOP Publishing | International Atomic Energy Agency
Nuclear Fusion
Nucl. Fusion **64** (2024) 096004 (13pp)
https://doi.org/10.1088/1741-4326/ad6014

Plasma performance and operational space with an RMP-ELM suppressed edge

C. Paz-Soldan[1,*], S. Gu[2,3], N. Leuthold[1,2], P. Lunia[1], P. Xie[3], M.W. Kim[4], S.K. Kim[5], N.C. Logan[1], J.-K. Park[6], W. Suttrop[7], Y. Sun[3], D.B. Weisberg[8], M. Willensdorfer[7], the ASDEX Upgrade Team[a], the DIII-D Team[b], the EAST Team[c] and the KSTAR Team[d]

[1] Department of Applied Physics & Applied Mathematics, Columbia University, New York, NY, United States of America
[2] Oak Ridge Associated Universities, Oak Ridge, TN, United States of America
[3] Institute of Plasma Physics, Chinese Academy of Sciences, Hefei, China
[4] Korea Institute of Fusion Energy, Daejon, Korea, Republic Of
[5] Princeton Plasma Physics Laboratory, Princeton, NJ, United States of America
[6] Department of Nuclear Engineering, Seoul National University, Seoul, Korea, Republic Of
[7] Max-Planck-Institut fur Plasmaphysik, EURATOM Association, Garching, Germany
[8] General Atomics, San Diego, CA 92121, United States of America

E-mail: carlos.pazsoldan@columbia.edu

Received 6 March 2024, revised 5 June 2024
Accepted for publication 8 July 2024
Published 23 July 2024

Abstract

The operational space and global performance of plasmas with edge-localized modes (ELMs) suppressed by resonant magnetic perturbations (RMPs) are surveyed by comparing AUG, DIII-D, EAST, and KSTAR stationary operating points. RMP-ELM suppression is achieved over a range of plasma currents, toroidal fields, and RMP toroidal mode numbers. Consistent operational windows in edge safety factor are found across devices, while windows in plasma shaping parameters are distinct. Accessed pedestal parameters reveal a quantitatively similar pedestal-top density limit for RMP-ELM suppression in all devices of just over 3×10^{19} m^{-3}. This is surprising given the wide variance of many engineering parameters and edge collisionalities, and poses a challenge to extrapolation of the regime. Wide ranges in input power, confinement time, and stored energy are observed, with the achieved triple product found to scale like the product of current, field, and radius. Observed energy confinement scaling with engineering parameters for RMP-ELM suppressed plasmas are presented and compared with expectations from established H and L-mode scalings, including treatment of uncertainty analysis. Different scaling exponents for individual engineering parameters are found as

---

[a] See Zohm *et al* 2024 (https://doi.org/10.1088/1741-4326/ad249d) for the ASDEX Upgrade Team.
[b] See Holcomb *et al* 2024 (https://doi.org/10.1088/1741-4326/ac301f) for the DIII-D Team.
[c] See Gong *et al* 2024 (https://doi.org/10.1088/1741-4326/ad4270) for the EAST Team.
[d] See Ko *et al* 2024 (https://doi.org/10.1088/1741-4326/ad3b1d) for the KSTAR Team.
[*] Author to whom any correspondence should be addressed.

1741-4326/24/096004+13$33.00 Printed in the UK

compared to the established scalings. However, extrapolation to next-step tokamaks ITER and SPARC find overall consistency within uncertainties with the established scalings, finding no obvious performance penalty when extrapolating from the assembled multi-device RMP-ELM suppressed database. Overall this work identifies common physics for RMP-ELM suppression and highlights the need to pursue this no-ELM regime at higher magnetic field and different plasma physical size.

Keywords: tokamak, edge localized mode, ELM suppression

(Some figures may appear in colour only in the online journal)

1. Introduction and motivation

Extrapolation of the tokamak approach to fusion energy production is challenged by the repetitive edge localized mode (ELM) instability [1, 2]. This instability is driven by edge gradients, and at reactor scale delivers a damaging heat and particle load to the first-wall [3–6]. The ELM also poses a risk to stable plasma operation due to high-Z wall material ingress into the plasma [7–9]. For this reason, ELM control is considered essential to operate at sufficient plasma current to achieve the ITER $Q = 10$ mission [10, 11].

ELM suppression by resonant magnetic perturbations (RMPs) is a primary technique to control the ELM in ITER, and the physics of RMP-ELM suppression has recently been thoroughly reviewed in [12] and before that in [13]. With the RMP technique, application of $\approx$0.1% level non-axisymmetric fields from nearby window-pane coils maintains a fully formed pedestal yet prevents the ELM—but only if certain access criteria are met. When RMP-ELM suppression is achieved, enhanced transport is observed, arising from either: parallel transport across macroscopic large-scale pedestal-top magnetic islands [14–17]; increased turbulent fluctuation levels directly arising from field penetration [18–20]; increased turbulence arising indirectly from penetration-induced changes to the radial electric field structure [21, 22]; or a combination of these effects. Additional mechanisms for RMP-ELM suppression have also been proposed, such as neoclassical transport effects [23, 24] or localized peeling-ballooning instabilities driven by 3D equilibrium modifications [25–28]. These mechanisms do not require significant field penetration, and as such struggle to explain the pedestal bifurcation from RMP-ELM mitigation into full ELM suppression [15].

After its initial discovery in DIII-D in 2003 [29–32], RMP-ELM suppression has been exported to tokamaks worldwide, and RMP coilsets have been incorporated into the ITER design [33, 34]. RMP coils are also planned for ELM control in SPARC [35]. In KSTAR, RMP coils with a unique engineering design were installed in 2008 [36], H-mode operation was established in 2010, and RMP-ELM suppression accessed in 2011 [37]. In AUG, the RMP coil system was installed in two stages between 2010–2011 [38]. Following improvements in scenario development to access low-collisionality pedestal regimes together with an increase in the plasma triangularity, full ELM suppression on AUG was accessed in 2016 [39, 40]. In EAST, RMP coils were installed in 2014 [41] and RMP-ELM suppression was accessed in dedicated experiments in 2015 [42]. The geometry of these devices, including their RMP coils, is presented in figure 1. Resulting from concerted effort over many years, the access to RMP-ELM suppression in different tokamaks worldwide offers a unique opportunity to explore cross-machine comparison and projection of the RMP technique, which this study begins to undertake.

It should also be noted that RMP coils have been installed in devices achieving plasma currents in the mega-Amp range without yielding access to RMP-ELM suppression. Databases for these devices with RMP coils active but with persistent ELMs have not been compiled and are beyond the scope of this work. Briefly, however, it can be said that these devices fall into two categories. First, devices with distant RMP coils that couple poorly to the edge resonant surfaces, such as JET [43, 44] and Alcator C-mod [45]; and second, the spherical tokamak devices MAST(-U) [46] and NSTX(-U) [47], for which the absence of RMP-ELM suppression is not yet understood. RMP-ELM suppression has also not been achieved in devices with currents well below a mega-Amp, presumably because sufficiently collisionless conditions cannot be achieved at that scale.

A first goal of this work is to document and compare the operational space accessed by tokamak plasmas with RMP-ELM suppressed edges. It is known that access to this regime requires specific operational criteria. However, after dedicated experimentation, the regime has been found on several tokamak devices worldwide. Each device exploring RMP-ELM suppression has unique characteristics, thus comparing the operational space can reveal areas of universality for RMP-ELM suppression, as well as areas of discrepancy. Furthermore, since many engineering parameters vary significantly across these devices, exploration of the plasma performance in terms of confinement and triple product [48] metrics can reveal empirical trends. Exploring these trends is a second goal of this work, alongside performing engineering regressions of the global confinement time to compare to trends in the established H- and L-mode scalings.

While this work focuses on RMP-ELM suppression, this is only one technique among several being explored to achieve ELM control in ITER, SPARC, and future reactors. These other approaches (such as Quiescent H-mode, Improved confinement I-mode, Enhanced D-alpha mode, and small/grassy

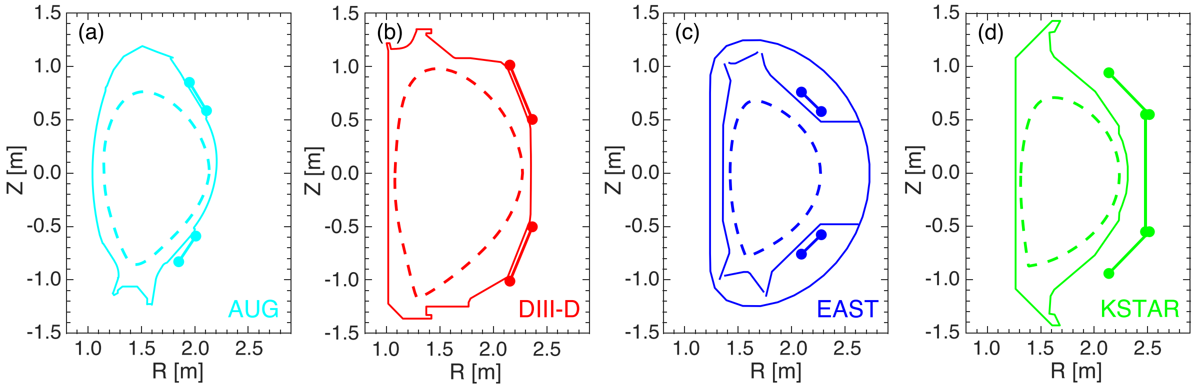

Figure 1. Comparison of vacuum vessel, RMP coil, and typical plasma geometry of the mid-scale tokamak devices that are the focus of this study: (*a*) AUG, (*b*) DIII-D, (*c*) EAST, (*d*) KSTAR.

ELM regimes) have been well-reviewed in the literature [49, 50]. A comparison of the operating space and plasma performance in DIII-D of the various no-ELM regimes has also been published recently [51]. Additionally, a similarly motivated multi-device comparison of I-mode can be found in the literature [52].

Criteria for inclusion of a datapoint into this database are largely the same as was elaborated in [51], where a detailed discussion of each criteria is included. A key criteria is stationarity, judged manually via the identification of stationary phases where parameters are roughly constant. The stationarity filter results in a subset of RMP-ELM suppressed points being retained. Additionally, machine parameters (field, current, power) must be fixed, ELMs must not be present during the time window (ie, full RMP-ELM suppression), and the time windows must be longer than approximately three energy confinement times. Finally, all data presented is from deuterium main-ion plasmas.

Furthermore, this work has endeavored to be as comprehensive as feasible. For AUG and EAST, new databases were populated by examining every RMP-ELM suppressed discharge since the discovery of the regime on those devices (2015 on EAST, 2016 on AUG) until 2020. This resulted in ≈200 stationary phases for AUG, and ≈250 stationary phases for EAST. For KSTAR, the database first presented in [53] was reused for this work, and the equilibria were recomputed using improved sensor compensation techniques. This KSTAR database features a comprehensive survey of ELM-suppressed discharges from 2016–2019. For DIII-D, the database first presented in [51] is reused. Owing to the maturity of the RMP technique in DIII-D, it is impractical to survey every RMP-ELM suppressed discharge, of which several thousand qualify. Instead, a curated subset of discharges highlighting variations in operating space and plasma performance is presented. Additionally, in some figures, data from an existing global database of type-I ELMing discharges in H-mode will be shown. This 'DB4v5' database was not prepared for this study, but rather it was curated by the International Tokamak Physics Activity (ITPA) for the improvement of the standard H_{H98y2} confinement scaling law [54].

The organization of this paper is divided into an exposition of the RMP-ELM suppressed operating space in section 2 and a discussion of observed plasma performance and confinement scaling in section 3. The operating space is presented in terms of basic machine parameters (section 2.1), RMP coil settings (section 2.2), pedestal parameters (section 2.3), and finally electron heating (section 2.4). The plasma performance is discussed in terms of normalized performance (section 3.1), absolute performance (section 3.2), and confinement time scaling (section 3.3). Discussions and conclusions are given in section 4.

2. RMP-ELM suppressed operating space

Observations in terms of machine parameters, RMP coil settings, pedestal parameters, and electron heating response are described sequentially to document the plasma operating space with an RMP-ELM suppressed edge. Since each datapoint is a stationary window with an RMP-ELM suppressed edge, the presented figures can be interpreted as windows of RMP-ELM suppression amidst a background of ELMing datapoints that are generally not shown. In some plots, the operating space is defined by the return of the ELM, while in others, it represents a more fundamental limitation of device capability. Note discussion of divertor integration, while found in [51] for DIII-D, is outside of the scope of this work. This is because divertor studies are idiosyncratic due to the variable divertor geometries found across devices. In contrast, the parameters highlighted here are expected to be more generically representative of the RMP-ELM suppressed edge.

2.1. Basic machine and shaping parameters

The operating space in terms of toroidal current (I) and toroidal field (B) is shown in figure 2(a). When considering all devices, a fairly wide range of values in both of these parameters is found. However, individual devices see more limited access to RMP-ELM suppression. DIII-D data reveals a relatively fixed ratio of I to B, indicative of a narrow range

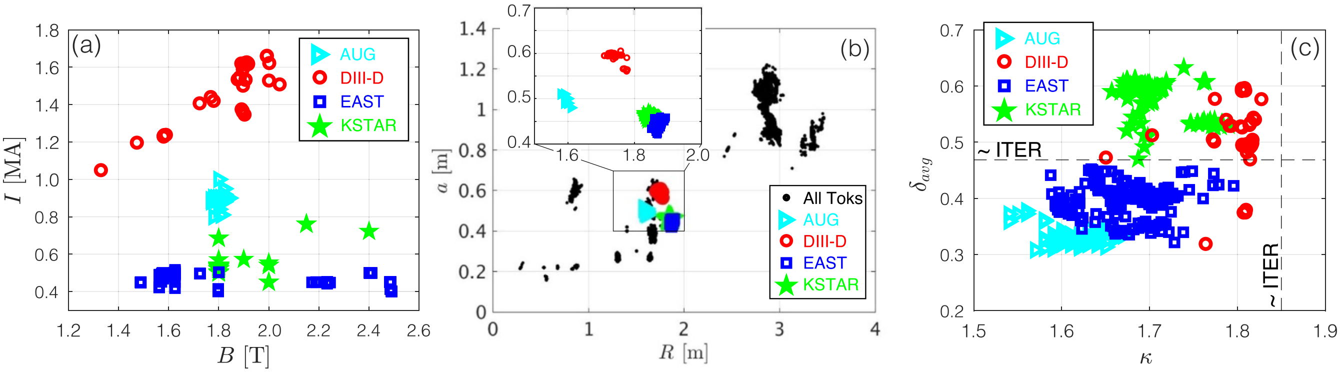

Figure 2. Operating space with an RMP-ELM suppressed edge in terms of (*a*) toroidal current (I) and toroidal magnetic field (B), (*b*) major radius (R_0) and minor radius (a), (*c*) elongation (κ) and average triangularity (δ_{avg}). RMP-ELM suppressed operating points are in color, while an ELMing database is shown as black dots [54].

of safety factor (q_{95}, from ≈3–4) owing to well known resonant window requirements [40, 55, 56]. AUG thus far has accessed the regime in only a limited range of I and B, which is partially related to the constraints imposed by central electron heating for high-Z impurity exhaust [57]. EAST is able to access RMP-ELM suppression over a range of B, but tends to favor operation in a more limited range of I. The limited I range in EAST is more reflective of the typical operational scenarios developed for that device as opposed to a fundamental physics limit. KSTAR has explored the most decoupled ranges of I and B [58].

Unlike the fairly wide variability in I and B, figure 2(*b*) illustrates the degree to which geometric size of all devices accessing RMP-ELM suppression is rather similar. AUG, DIII-D, EAST, and KSTAR are all mid-scale tokamaks with conventional aspect ratio, and as illustrated occupy a narrow range compared to the worldwide database. As will be shown, this fact is a key limitation of worldwide RMP-ELM suppression research and strongly motivates the inclusion of RMP coils into future devices of different size, such as ITER [33, 59, 60] and JT-60SA [61, 62]. When considering the regression analysis presented in section 3.3, no size scaling will be possible. The inset in figure 2(*b*) does show some modest variation in aspect ratio, which will be shown later to lead to variations in I/aB at constant q_{95}.

A more varied picture is found in terms of plasma shaping, which covers a wide range due to variations both across as well as within machines. While RMP-ELM suppression is accessed over a wide range of shapes, individual devices find strong shaping thresholds [63, 64]. DIII-D has reported a δ_{avg} threshold above which no RMP-ELM suppression is found [65], while a lower δ_{avg} threshold below which no suppression is found is reported in AUG [39, 40]. In EAST and KSTAR, progressing towards double-null divertor shapes also raises δ_{avg}, with an upper limit in δ_{avg} near DND shapes reported [66]. It is at present unclear if δ_{avg} plays a role in this threshold or if this physics might be responsible for the difficulties seen in spherical tokamaks. Thus far, no reports of thresholds in κ have appeared in the literature. Due to its shape flexibility, DIII-D has reported RMP-ELM suppression in plasmas closely matching ITER's κ, δ_{avg}, I/aB, and q_{95} [67].

2.2. RMP coil configurations and safety factor windows

Each of the different experiments also feature different geometries of RMP coils, shown already in poloidal cross-section in figure 1. Both AUG and EAST are equipped with two toroidal rows of 8 RMP coils each, above and below the midplane, favoring $n = 2, 4$, where n is the toroidal mode number of the applied RMP field. DIII-D is equipped with two similar rows, but with 6 coils each (favoring $n = 3$). KSTAR has three toroidal rows, each with 4 coils, thus favoring $n = 1, 2$ [68]. As can be seen in figure 3(*a*), access to RMP-ELM suppression differs in n-number and q_{95} across devices. Access with $n = 2, 3$ [15, 69, 70] has been observed in DIII-D, but not $n = 1$. AUG has thus far accessed RMP-ELM suppression with only $n = 2$. KSTAR's RMP coils are capable of both $n = 1, 2$, and both have been used to access RMP-ELM suppression. The EAST RMP coils are capable of $n = 1, 2, 3, 4$, and all have been used to access RMP-ELM suppression. As can be seen, low-n RMPs favor RMP-ELM suppression at high q_{95}, while high-n favors low q_{95}. This is because the coupling to the resonant surfaces is poor for high-n RMPs at high q_{95} [71], while low-n RMPs risk driving disruptive $m/n = 2/1$ tearing instabilities at low q_{95}, requiring careful tuning of the poloidal spectrum [72, 73]. Note variations in the poloidal spectrum are not here further discussed, as the spectra to achieve the most favorable results is specific to each device's RMP coil geometry. Results further depend on whether the goal is simply maximizing the coupling to edge resonant surfaces, or reducing core surface coupling whilst maintaining sufficient edge coupling [72, 74–78].

Figures 3(*a*) and (*b*) both show clear windows in q_{95}, inside of which RMP-ELM suppression is possible. The window behavior in q_{95} is a classic signature of the RMP-ELM suppression phenomenon [79, 80], which has been recovered by simulations considering the alignment of the edge rational surface with the pedestal-top region [81, 82]. This alignment requirement indicates that the transport enhancement responsible for RMP-ELM suppression is linked to the position of the rational surface, as enhancing the transport in the pedestal-top region should prevent gradient formation towards the peeling ballooning stability limit [83]. The alignment picture for the

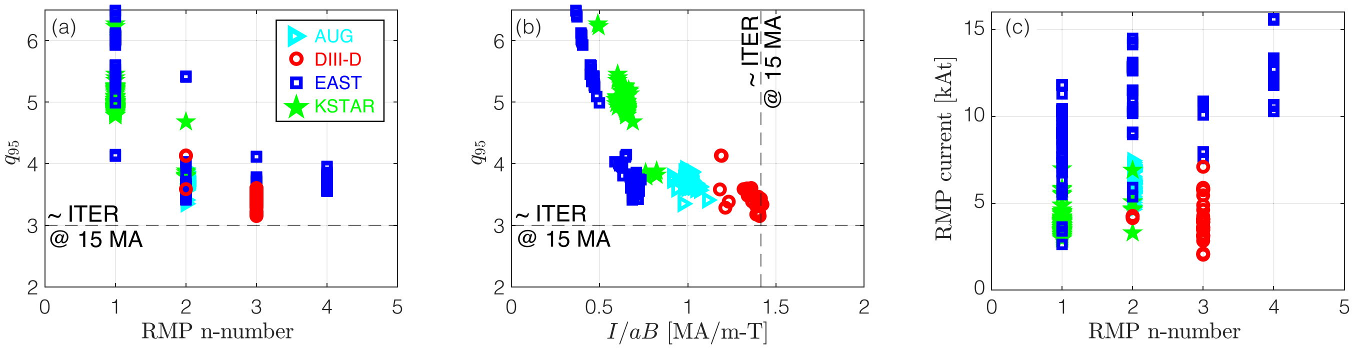

Figure 3. RMP-ELM suppression window dependence on (*a*) RMP toroidal mode 'n-number' and edge safety factor (q_{95}), (*b*) normalized current (I/aB) and q_{95}, and (*c*) RMP n-number and RMP coil current. Different devices can use different n-numbers based on the number of coils per toroidal row.

q_{95} window however fails to capture all aspects of the data, such as for example the fact that some q_{95} windows appear far more robust than adjacent ones. Each device has gaps in q_{95} where RMP-ELM suppression is not achieved, though when considering all devices a wide range of q_{95} values over which RMP-ELM suppression is observed. Both DIII-D and AUG have not yet accessed full RMP-ELM suppression at high q_{95}, though DIII-D achieved type-I RMP-ELM suppression at $q_{95} = 7$ [84] with $n = 3$ fields (not shown). In the range of q_{95} 4.8–6.2 is also where AUG first discovered strong ELM mitigation [85]. Note very recent EAST data, taken after the compilation of this database, has extended $n = 4$ RMP-ELM suppression to $q_{95} \approx 3$ [86] and $q_{95} > 4$, with different q_{95} gap sensitivity observed [87]. Also interesting is the generic accessibility of a window between $q_{95} = 3$–4. From the range of I/aB presented it can be surmised that q_{95} is an appropriate characterization of the operating window, since the window does not depend strongly on I/aB (ie, it is invariant with aspect ratio).

It is also illustrating to consider the RMP current (in absolute kAt units) required to access RMP-ELM suppression in these devices. Naturally, the coilsets are not equivalent in terms of their propensity to create the 3D topology necessary for ELM suppression. This is consistent with a very wide spread of RMP coil currents, and motivates a more physics-informed treatment of the RMP coil amplitude and coupling effects in the future.

2.3. Pedestal parameters and density limits

Comparing pedestal parameters reveals consistent density limits and a wide range of other parameters. As a prelude, figure 4(*a*) compares the pedestal pressure p_{ped} to the volume-average pressure ($\langle p \rangle$). Note p_{ped} is taken to be $2p_{\mathrm{e,ped}}$ as measured by Thomson scattering or ECE, which is more experimentally reliable and is expected to be accurate in reactor conditions. All devices except DIII-D are seen to operate in relatively narrow ranges of $\langle p \rangle$, ordered by the I accessible within each device. A surprising result is that no significant correlation is seen between p_{ped} and $\langle p \rangle$ in each device, with a relatively wide range of p_{ped} not significantly levering $\langle p \rangle$. This is contrary to the expectation that maximizing the pedestal optimizes the global performance [88], and indicates distinct core confinement physics plays an important role in the global performance. Indeed, as will be explored in section 3, this data hints at the important role of I in setting the global performance.

A closer look at the electron pressure is shown in figure 4(*b*), by comparing the contribution from the pedestal-top electron density ($n_{\mathrm{e,ped}}$) and temperature ($T_{\mathrm{e,ped}}$). The lower limit of these parameters is set by the L-H or H-L transition. A key finding arising from this work is that there is a consistent upper $n_{\mathrm{e,ped}}$ limit found across all devices, which is particularly remarkable given the ranges of other parameters existing in the multi-device dataset. This will be discussed further in section 4. Another interesting finding is that the $\langle p \rangle$ ordering seen in figure 4(*a*) is recovered in $T_{\mathrm{e,ped}}$. Each device, however, spans a range of $n_{\mathrm{e,ped}}$, and as expected $T_{\mathrm{e,ped}}$ can be higher when $n_{\mathrm{e,ped}}$ is lower.

One of the classic representations of the RMP-ELM suppression operating space is in $n_{\mathrm{e,ped}}$ and pedestal-top electron collisionality [89] (where ν_{e}^* is computed using the equation found in [90]), reproduced in figure 4(*c*). Recall type-I ELM suppression can also be found at high $n_{\mathrm{e,ped}}$ and ν_{e}^* in AUG [85] and DIII-D [30] (though small ELMs remain), but this data is not included in this database, which looks at suppression of all ELMs. An interesting result is the wide access in ν_{e}^* found in EAST and KSTAR, indicating perhaps a continuous transition between the low ν_{e}^* and high ν_{e}^* regime in those devices. Note the relative scarcity of intermediate $n_{\mathrm{e,ped}}$ points in KSTAR is thought to be due to sampling bias as opposed to a difficult to access region.

A final pedestal factor explored is the relationship of the exhaust power (P_{net}) to the H-mode power threshold $P_{\mathrm{net}}/P_{\mathrm{LH08}}$, where the LH08 scaling is taken from [91]. In figure 4(*d*) this is plotted against the average density $\langle n_{\mathrm{e}} \rangle$. It can be seen that DIII-D and AUG operate at overall higher $P_{\mathrm{net}}/P_{\mathrm{LH08}}$, and that a decreasing trend is seen as $\langle n_{\mathrm{e}} \rangle$ is rising. This is in part due to the inverse dependence of $\langle n_{\mathrm{e}} \rangle$ in the LH08 power threshold scaling (P_{net} itself does not fall with $\langle n_{\mathrm{e}} \rangle$), but it does illustrate that the RMP-ELM suppression phenomenon appears to exist at the approximate location that the low density branch of the H-mode threshold would be expected to exist [92]. Since the database does not contain

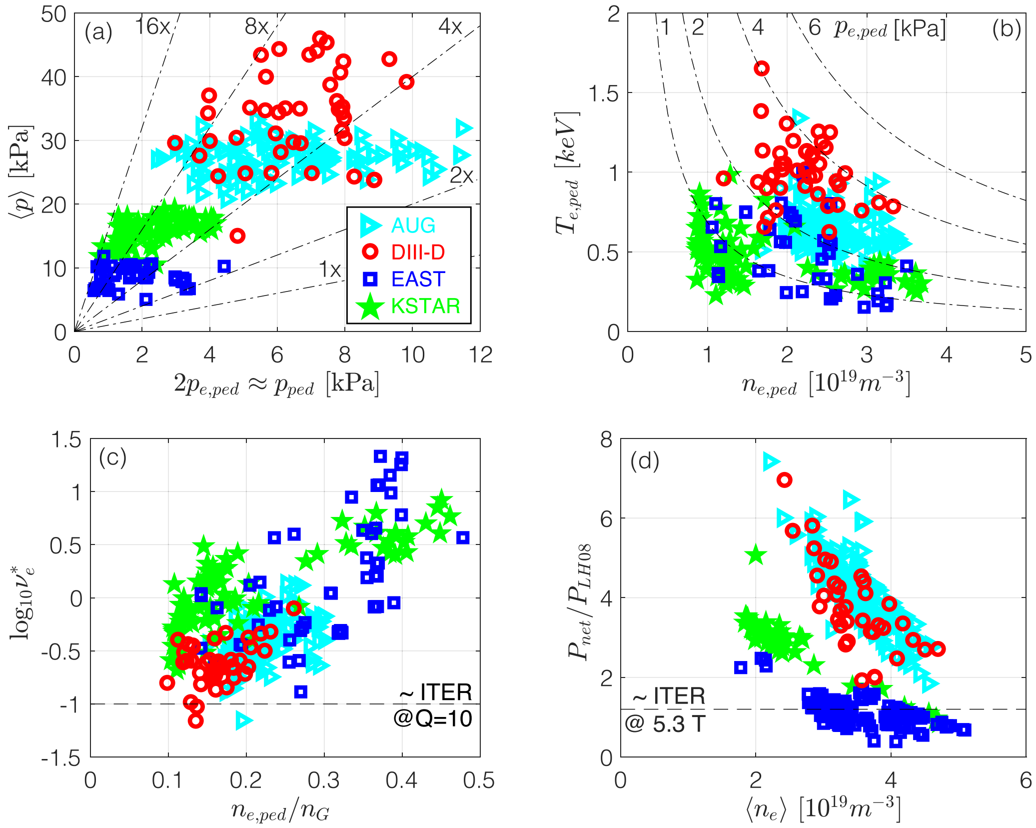

Figure 4. Pedestal parameters during RMP-ELM suppression. (*a*) A wide range of pedestal pressure (p_{ped}, taken as twice the electron pedestal pressure $p_{\mathrm{e,ped}}$) with relatively invariant average pressure $\langle p \rangle$. (*b*) Operating space of pedestal electron density ($n_{\mathrm{e,ped}}$) and temperature ($T_{\mathrm{e,ped}}$). (*c*) Pedestal-top electron collisionality (ν_e^*) and $n_{\mathrm{e,ped}}$ (normalized to the Greenwald density n_{G}), and (*d*) exhaust power divided by L-H threshold power ($P_{\mathrm{net}}/P_{\mathrm{LH08}}$) plotted against line-average density ($\langle n_{\mathrm{e}} \rangle$).

corresponding L-mode points, it cannot be used to identify the L-H transition for these conditions.

2.4. Limits to electron heating

Integration of RMP-ELM suppression with electron cyclotron heated (ECH) plasmas is presented in figure 5. ECH will be the dominant power source for ITER pre-fusion power plasmas [93] as well as a reasonable substitute for bulk plasma heating from fusion-born alpha particles. This distinction is important because electron heating significantly modifies the turbulent transport properties of plasmas [94–99]. The importance of this physics is well appreciated, motivating worldwide studies of the impact of dominant electron heating on the RMP-ELM suppression scenario, often limited by the availability of sufficient P_{ECH}, as quantified in figure 5(*a*), where $P_{\mathrm{ECH}}/P_{\mathrm{tot}}$ is always rather low P_{ECH} in this dataset is injected at various radii, though always inside of the pedestal-top region.

On AUG, which has achieved the highest absolute P_{ECH} and $P_{\mathrm{ECH}}/P_{\mathrm{tot}}$, there is evidence for a loss of RMP-ELM suppression at the highest $P_{\mathrm{ECH}}/P_{\mathrm{tot}}$ (around 0.5). However, DIII-D has not yet identified an operational limit within the range of P_{ECH} injected [67]. EAST has similarly not found a limit with P_{ECH}, and considering wave heating from lower hybrid and ion cyclotron heating, has accessed RMP-ELM suppression in fully wave-heated discharges [42]. Experiments at KSTAR are ongoing with findings still to be reported [100]. Considering the pedestal impact of P_{ECH}, figure 5(*b*) shows a high proportion of the data exists at relatively high ion temperature (T_{i}) as compared to T_{e}, again indicating a preponderance of data with strong ion heating and potentially also significant main ion fuel dilution. Interestingly, AUG has previously reported an operational boundary when T_{i} falls below T_{e} [40], and the origin of this continues to be investigated.

3. Plasma performance with an RMP-ELM suppressed edge

The plasma performance of discharges with RMP-ELM suppressed edges is surveyed, first in terms of normalized parameters such as confinement quality factors (H_{H98y2}, H_{L89}) and normalized pressure (β_{N}), followed by absolute performance metrics such as the average pressure ($\langle p \rangle$) and confinement time (τ_{E}). Due to the wide range of I, B, $\langle n_{\mathrm{e}} \rangle$, and P_{tot} available, scaling against these parameters is pursued to provide insight on the confinement extrapolation to future devices.

3.1. Normalized performance

The core stability of tokamak plasmas is classically represented by the Troyon stability diagram, [101], shown in figure 6(*a*). These diagrams plot the toroidal beta (β_{T}) against

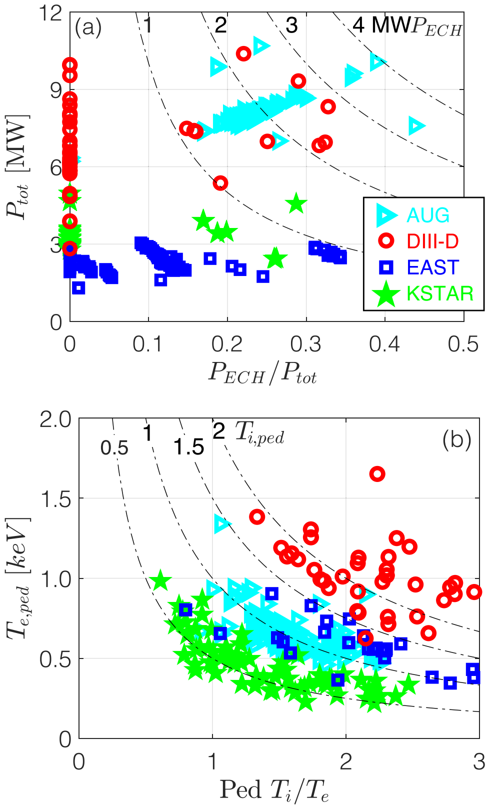

Figure 5. Integration with electron heating: (*a*) operational space in terms of the ratio of ECH heating (P_{ECH}) to total input power (P_{tot}) plotted against P_{tot} with dashed lines at constant P_{ECH}. (*b*) Most data exists at high ion to electron temperature ($T_{\mathrm{i}}/T_{\mathrm{e}}$), owing to a relative lack of P_{ECH}.

the normalized current (I/aB) with diagonal dashed lines representing the normalized beta (β_{N}). The RMP-ELM suppressed data occupies a region of the Troyon diagram at intermediate β_{N}, with lower values presumably falling into L-mode, and higher values limited by stability or confinement. Across all devices a wide range of I/aB is found, as was also shown in figure 3(*b*). Overall the normalized stability of RMP-ELM suppressed plasmas in terms of these parameters is consistent with the requirements of ITER as indicated by the dashed lines.

Normalized plasma performance is usually described in terms of the confinement quality 'H-factor'. Figure 6(*b*) highlights the normalized pressure (β_{N}) against the H-factor derived for L-mode plasmas (H_{L89}) [102]. The H_{L89} data highlights the typically seen intermediate level of confinement between L-mode ($H_{\mathrm{L89}} \approx 1$) and H-mode ($H_{\mathrm{L89}} \approx 2$). The H_{L89} factors also span a wide range in any individual device, that is overall between $\approx$1 and 2 for all devices. A strong correlation of β_{N} and H_{L89} is seen in each device, indicating power degradation is not as severe as expected by the H_{L89} law. Section 3.3 will use this data to explore the validity of the H_{L89} scaling law for these plasmas and to discuss extrapolation to next-step devices. A notable feature is the presence of two clusters of EAST data, with the lower β_{N} cluster being the lower power dominantly wave-heated discharges, motivating additional studies on the optimization of the RMP-ELM suppression scenario in these conditions. Very recently, and after the compilation of this database, higher β_{N} values (2.65) have been achieved in KSTAR [103]. The $\beta_{\mathrm{N}} = 1.8$ target of ITER is well within the multi-device dataset and is approximately accessed by all devices.

Comparison to the H-mode 'H98y2' scaling law [104] is presented in figure 6(*c*). Similar trends in confinement quality between H_{H98y2} and H_{L89} are observed, and again the requisite values for ITER are well within the multi-device database. Section 3.3 will explore extrapolation based on the observed $\tau_{\mathrm{E,th}}$ and H-mode expectations. Note presenting H_{H98y2} values requires computing the fast ion fraction, which will be shown in section 3.3 to be a key uncertainty. For DIII-D and AUG, automated between-shot transport routines [105, 106] extract the fast ion pressure and are expected to be fairly robust. For EAST, which is dominated by radio-frequency heating, a fast-ion fraction of 0% is assumed. For KSTAR, the fast ion fraction is taken to be uniformly 40%, in line with previous transport calculations [107, 108].

3.2. Absolute performance

While normalized plasma performance naturally compares the data to the expectations of plasma stability and confinement quality, this approach can also mask underlying trends. Discussion of the absolute plasma performance offers additional insight. The most straight forward way to measure plasma performance is Lawson's triple product [48], here taken as $\langle p\rangle\tau$, which substitutes the average pressure for the more direct core ion temperature and fuel density. $\langle p\rangle\tau$ is more robust across the multi-device dataset, and further removes some bias towards highly peaked profiles, which may be more reactive in the core, but would produce less fusion power overall.

The triple product $\langle p\rangle\tau$ can be separated into its constituent $\langle p\rangle$ and τ_{E}, as shown in figure 7(*a*). An interesting feature is the different relative mixes of $\langle p\rangle$ and τ_{E} across devices, and in particular all devices except DIII-D occupy predominantly similar τ_{E} ranges. These results motivate a regression analysis on the observed confinement, which is the subject of section 3.3. Already, it can be seen that the performance data is roughly ordered by *I*. Also interesting is the clustering of data from each device with relatively little overlap. The clustering highlights the important role of the operational space in the observed performance, where narrow operational windows result in clustered performance data. This will be further elaborated in section 4. Considering the highest $\langle p\rangle\tau$ discharges in DIII-D, they are achieved by exploiting hysteresis in the bifurcation into RMP-ELM suppression, reducing the RMP current after ELM suppression is accessed [109]. Note the $\langle p\rangle\tau$ required for net energy gain and ignition is several atmosphere-seconds, varying based on the ion temperature [110].

A valuable normalization metric for $\langle p\rangle\tau$ is found to be *IaB*, the product of the plasma current (*I*), minor radius (*a*), and toroidal field (*B*) and which has the units of force [MN] [111]. As shown in figure 2, *a* is similar across devices, while *B* varies

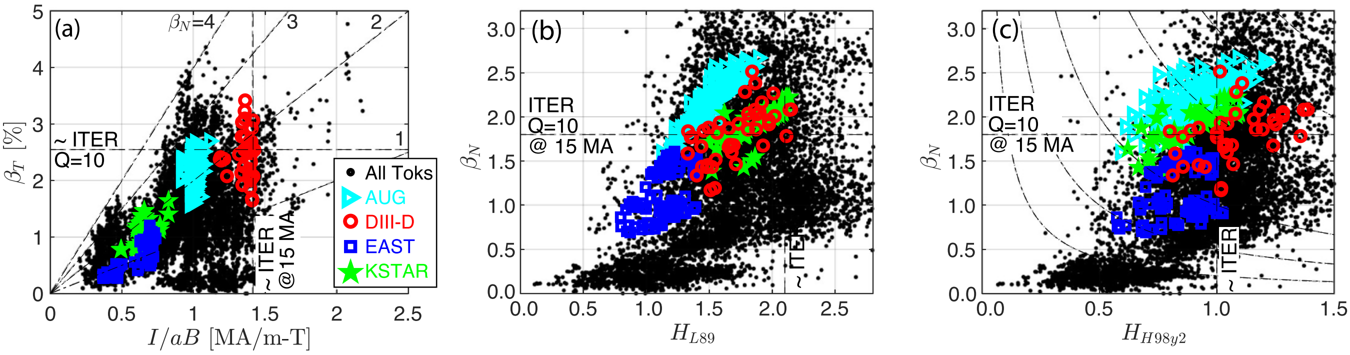

Figure 6. Normalized plasma performance in terms of (*a*) Troyon core stability given by toroidal beta (β_T) and normalized current (I/aB) with dash-dot lines indicating constant normalized pressure (β_N). Confinement quality factors using (*b*) L-mode scaling laws (H_L89) or (*c*) H-mode scaling laws (H_H98y2) as a function β_N. Dashed lines indicate ITER 15 MA $Q = 10$ targets. Data from the global tokamak database is also included.

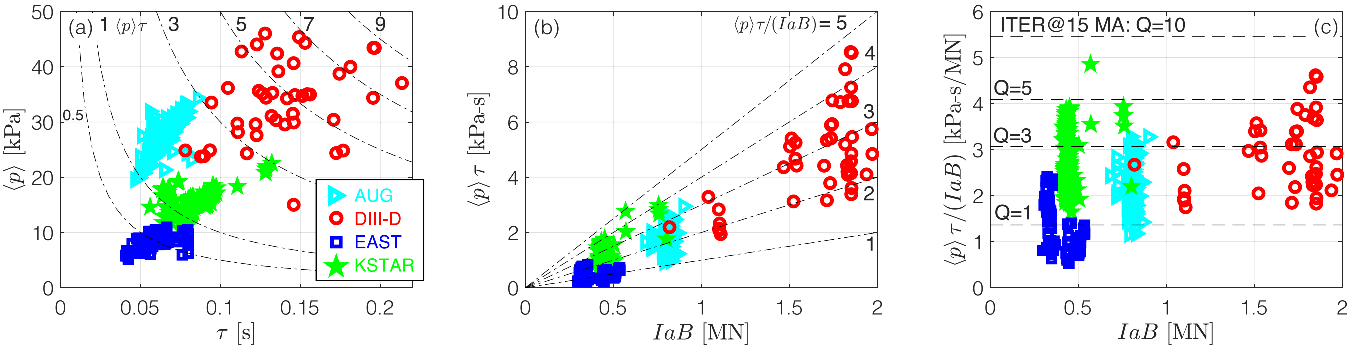

Figure 7. Absolute plasma performance represented by: (*a*) average pressure ($\langle p\rangle$) and confinement time (τ_E), with dash-dot lines at constant triple product ($\langle p\rangle\tau$). (*b*) Triple product $\langle p\rangle\tau$ referenced to IaB, showing an increasing trend. (*c*) $\langle p\rangle\tau$ normalized to IaB referenced to IaB. Dashed lines reference fusion gain Q values at 15 MA in ITER.

over about a factor of 2, and I especially varying over a factor of 4, yielding an overall 7x variation in IaB. This normalization metric also highlights the rather large extrapolation to ITER ($IaB \approx 160$), and SPARC ($IaB \approx 60$). Perhaps surprisingly, as shown in figure 7(*b*) the peak $\langle p\rangle\tau$ is well-captured by the IaB normalization across the multi-device RMP-ELM suppression database, which is to say the peak $\langle p\rangle\tau$ values are found to increase with IaB. Further discussion of the $\langle p\rangle\tau/IaB$ metric is found in [51, 111].

Figure 7(*c*) shows the absolute fusion performance metric $\langle p\rangle\tau$ normalized against the IaB metric. Most data is found to occupy values of $\langle p\rangle\tau/IaB$ between 2 and 4. As with the β_N data in figure 6(*b*), there is a separate cluster of data from EAST which is distinct due to the dominant wave heating of those points, compared to the dominant NBI heating of the data from DIII-D, AUG, and KSTAR. Further, since the $\langle p\rangle\tau$ target for ITER operating at 15 MA is known [112] ($\tau_\mathrm{E,th} \approx 3$ s, stored energy ≈350 MJ, volume ≈840 $\mathrm{m^{-3}}$), as is the IaB, the $\langle p\rangle\tau/IaB$ parameter can be directly related to an expectation of the fusion gain, Q, which is also included in figure 7(*c*). This finds the peak fusion performance shy of the Q = 10 target, with the preponderance of data existing between $Q = 1$ and $Q = 5$. These projections are rather crude however, and should not be taken beyond the high-level conclusion that the absolute performance is in the range of what is needed for future devices such as ITER.

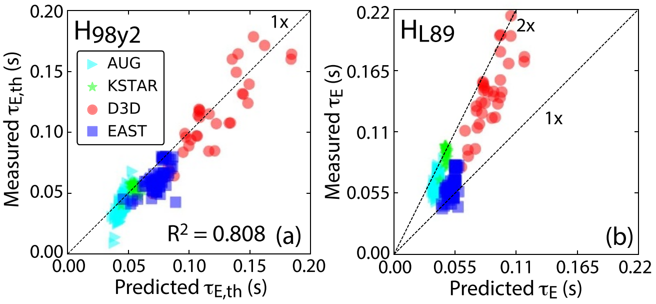

Figure 8. Comparison of measured $\tau_\mathrm{E,th}$ and τ_E to scaling law predictions for (*a*) H-mode and (*b*) L-mode.

3.3. Confinement scaling

Comparison of the observed confinement in RMP-ELM suppressed discharges is made to the well-established existing confinement scaling laws, and an assessment of improved scaling laws derived from the assembled databases is presented. Figure 8 presents the consistency of the RMP-ELM

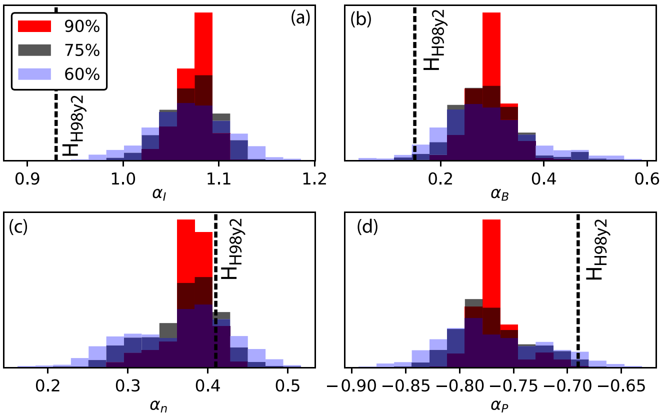

Figure 9. Probability density function (PDF) of the scaling law exponents for $\tau_{\mathrm{E,th}}$ in terms of (*a*) *I*, (*b*) *B*, (*c*) $\langle n_{\mathrm{e}} \rangle$ and (*d*) P_{aux}, upon randomly sampling 90%, 75%, and 60% of the full database. Dashed lines show expecatation from H_{H98y2}.

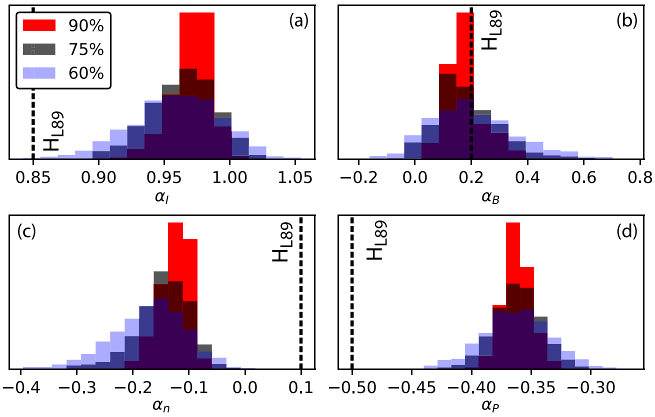

Figure 10. PDF of the scaling law exponents for τ_{E} in terms of (*a*) *I*, (*b*) *B*, (*c*) $\langle n_{\mathrm{e}} \rangle$ and (*d*) P_{aux}, upon randomly sampling 90%, 75%, and 60% of the full database. Dashed lines show expectation from H_{L89}.

suppressed experimentally measured confinement time with the predictions from the established H-mode H_{H98y2} scaling law [104, 113] and H_{L89} scaling law [102]. The H_{H98y2} scaling requires estimating the fast ion contribution to the stored energy. As discussed in section 3.1, the certainty in the fast ion fraction varies across the multi-device dataset, and the approximations for EAST and KSTAR taken in section 3.1 are retained. Within these uncertainties, a reasonable agreement is found with an R^2 value of 0.808 obtained. Turning to the H_{L89} scaling law [102], as was also shown in figure 6(*b*), the data is found to be intermediate between H_{L89} of 1 and 2 as indicated in figure 8(*b*). An increasing slope is found, with the larger absolute confinement times trending towards H_{L89} of 2. These observed differences in slope motivate exploring new scaling laws via engineering parameter regression for RMP-ELM suppressed plasmas [114]. Note uncertainty in the fast-ion fraction does not impact projections based on τ_{E} and H_{L89}.

Exponential scaling coefficients are derived by deploying linear least-squares fitting of the confinement times with fast ion correction ($\tau_{\mathrm{E,th}}$) and without (τ_{E}) to the logarithm of the engineering parameters of plasma current (*I*), toroidal field (*B*), average density ($\langle n_{\mathrm{e}} \rangle$), and auxiliary heating power (P_{aux}). To alleviate sampling bias present in the database, kernel density estimation is used to assign weights to data points such that poorly-sampled regions of the parameter space are weighted more strongly than highly-sampled regions [115]. Using this technique, exponential scaling coefficients α_I for *I*, α_B for *B*, α_n for $\langle n_{\mathrm{e}} \rangle$, and α_P for P_{aux} can be obtained. As shown in figure 2(*b*), there is minimal size variation across devices, thus no attempt is made to include geometry fitting terms. Further, as discussed in [114], engineering parameter regression underestimates the uncertainties involved, which arise not from the statistical goodness-of-fit, but rather from the completeness of the underlying databases. To present the confinement scaling results along with a realistic assessment of uncertainty, the fitted exponential scaling coefficients are presented statistically across many different regression attempts on randomly selected 90%, 75%, and 60% subsets of the full database prepared for this study. The motivation for repeating the regression analysis on randomized subsets of the data is to yield more representative uncertainty quantification than the error bars resulting from a single scaling law derived from the full (100%) dataset. The error bars on a single regression study of the full dataset scaling law are unrealistically low, as revealed by this alternative methodology.

Results are shown in figure 9 for $\tau_{\mathrm{E,th}}$ scaling along with the expectation from H_{H98y2}. Each randomized subset regression yields its own scaling exponents, which can vary significantly, and are thus presented as probability density functions. Notwithstanding the observed variability, some aspects appear robust in the present dataset: an approximately linear *I* scaling is revealed, along with an $\langle n_{\mathrm{e}} \rangle$ scaling consistent with H_{H98y2}, and a slightly stronger *B* dependence and more severe power degradation than expected from H_{H98y2} scaling.

Note that the scaling of $\tau_{\mathrm{E,th}}$ introduces uncertainty from the magnitude of the fast ion contribution, which is subtracted from the stored energy to arrive at $\tau_{\mathrm{E,th}}$. The sensitivity to the magnitude of the fast ion correction was explored in dedicated scans (not shown). For KSTAR, decreasing the fast ion fraction resulted in reduced R^2 values and a weaker exponent on fitted $\langle n_{\mathrm{e}} \rangle$. This sensitivity is due to KSTAR containing the lowest $\langle n_{\mathrm{e}} \rangle$ points in the entire multi-device database. For EAST, the R^2 value monotonically increased as the fast ion fraction decreased, supporting the choice of using no fast ions for the regression analysis. The power degradation and density exponent also increased as the EAST fast ion fraction decreased. Overall, the fast ion fraction is identified as a dominant uncertainty for the multi-device $\tau_{\mathrm{E,th}}$ and H_{H98y2} scaling exercises.

Scaling of τ_{E} and comparison to the H_{L89} scaling law avoids the uncertainty associated with determining the fast ion content. As shown in figure 10, some variation in scaling law exponent is found for τ_{E} regression as compared to $\tau_{\mathrm{E,th}}$ regression. The linear *I* dependence is preserved. A significantly weaker power degradation is found for τ_{E} as compared to $\tau_{\mathrm{E,th}}$, even in excess of the expectation from H_{H98y2} to H_{L89}. This

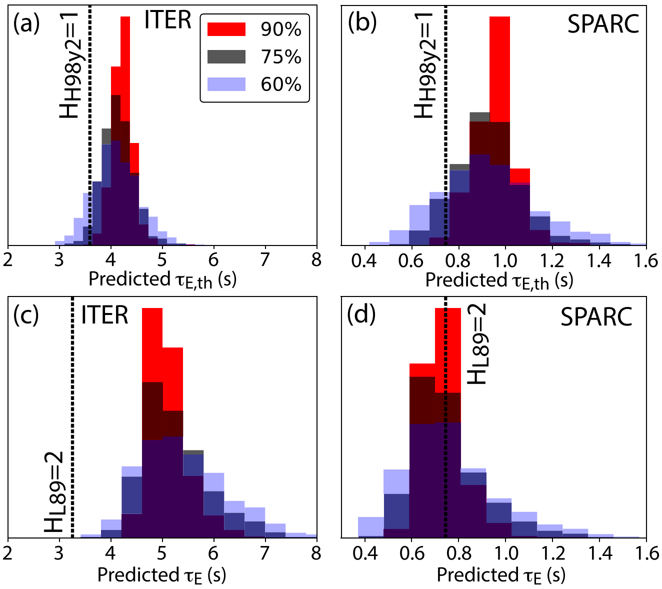

Figure 11. Extrapolation of $\tau_{\mathrm{E,th}}$ (figure 9) and τ_{E} scaling (figure 10) to ITER and SPARC parameters as compared to the existing $H_{\mathrm{H98y2}} = 1$ and $H_{\mathrm{L89}} = 2$ expectation, expressed as PDFs.

suggests much of the heating power goes into the fast ion population, which is not surprising given these are low density predominantly NBI-heated plasmas. Most surprising is the exponent on $\langle n_e \rangle$, which robustly is found to be weakly negative, in contrast to the weakly positive expectation from H_{L89}. The reason is not understood, though in absolute terms the difference from H_{L89} is no worse than in the other parameters.

With the same statistical approach used to describe the exponential scaling coefficients, the results of $\tau_{\mathrm{E,th}}$ (figure 9) and τ_{E} (figure 10) scalings are used to perform a projection to the upcoming tokamaks under construction, ITER [116] and SPARC [117], as shown in figure 11. In order to perform the extrapolation to ITER, physical size scaling exponents are taken from the pre-existing H_{H98y2} or H_{L89} scaling, introducing a significant uncertainty to those projections. Interestingly, this caveat is relatively unimportant for SPARC, since its physical size is comparable to the devices used in this regression. The standard isotope mass scaling is also used assuming a 50:50 deuterium tritium mix. For both devices, the $\tau_{\mathrm{E,th}}$ extrapolation is modestly above the existing projections from $H_{\mathrm{H98y2}} = 1$, but well within the uncertainties characterized by the randomized subsets. Thus, the variations in exponents seen in figure 9 are found to cancel out to some degree. Extrapolations based on τ_{E} scaling for SPARC (figure 11(*d*)) are also found to be fully overlapping with expectations, indicating cancellation of the density and power exponent deviations for that device. For ITER however (figure 11(*c*)), a significantly higher confinement time is predicted, likely due to the higher input power and lower density expected for that device. Also worth noting is the relatively large uncertainty for these projections, indicating the extrapolation is relatively unconstrained. Gaps in the input data utilized for the scaling exercises will be discussed in the following section. Despite the uncertainty, it is clear that the inclusion of an RMP-ELM suppressed edge did not produce dramatically pessimistic confinement projections for either ITER or SPARC.

Finally, a similar analysis was also conducted for regression analyses including the effect of plasma rotation, which is also available for a subset of the multi-device RMP database. While for brevity the results are not shown in detail, the generic effect of including rotation was found to be to reduce the power degradation extracted from the dataset. Instead, a positive correlation of the confinement with rotation was observed, with exponents in the range of 0.1–0.2 found. The utilization of these regressions for extrapolation requires an accurate assessment of the rotation expected in ITER and SPARC while the edge is RMP-ELM suppressed, a question which is still under active study [118, 119].

4. Discussion and conclusions

A remarkable finding of this effort is the consistency of the upper $n_{\mathrm{e,ped}}$ limit observed across all devices. The consistency is observed despite a wide range of machine parameters, RMP coil geometries, and operational scenarios. Considering individual devices such as DIII-D, differences in the $n_{\mathrm{e,ped}}$ threshold have been reported as $T_{\mathrm{e,ped}}$ is varied [63], however this does not extend to the full multi-device database. Unless the finding is coincidental, the commonality across devices suggests an important role for the device size or ρ_{i}^{*} in this limit. Taking the simplifying rough approximation that the separatrix density is proportional to $n_{\mathrm{e,ped}}$, the invariance of the $n_{\mathrm{e,ped}}$ threshold with I greatly facilitates divertor integration at low I. This is because the heat flux width scales inversely with I [120], spreading the divertor power dissipation over a wider area at low I (assuming fixed separatrix density). These dependencies provide an explanation for the relative difficulty of AUG and DIII-D achieving edge-integrated RMP-ELM suppression, as compared to EAST and KSTAR [40, 121, 122], though the dynamics of the seeded impurities also play an essential role in divertor integration [123, 124] as does the divertor geometry. Overall, additional effort is required to understand the $n_{\mathrm{e,ped}}$ threshold, as its scaling to ITER and future devices is the key question confronting the possibility of integrating a dissipative divertor with the RMP scenario in high current scenarios.

Considering the confinement scaling exercise, one key finding shown in figure 4(*a*) is the important role the core confinement (as opposed to the pedestal) is playing in the overall plasma performance of the RMP-ELM suppressed plasmas. This observation is thought to be related to the relatively low density of these plasmas, coupled with their neutral-beam injection (NBI) dominated heating mixes. NBI heating at low density tends to impart significant momentum to the plasma, bringing in additional dependencies to the confinement (such as core ExB shear [125, 126] and hot ion modes [94, 127, 128]) that are less likely to extrapolate to future devices. To address this issue, exploration of RMP-ELM suppression under dominant electron heated low input torque regimes is an active area of study in the world program, as described in section 2.4.

Another general observation from this exploration is the limitations in what can be achieved with multi-device comparisons when the device size is relatively similar, as was shown in figure 2(*b*). Engineering parameter regression cannot be extended to the major or minor radius, adding uncertainty to its use to extrapolate to ITER or other larger devices, though this is not an issue for SPARC. Installation of RMP coils on devices of larger major radius is essential for empirical extrapolation to ITER. This could be provided by JT-60SA in the coming years [61, 129]. Installation of RMP coils on a smaller high-field device, such as COMPASS-U [130, 131], would also improve the ability to conduct empirical extrapolations.

Acknowledgments

This work was the result of dedicated database extraction by the authors from AUG, DIII-D, EAST, and KSTAR. As such, the experimental teams from each of AUG, DIII-D, EAST, and KSTAR deserve explicit recognition for their efforts in producing the plasmas summarized here. Additionally, the authors thank Dr A.O. Nelson for assistance with database curation.

This material is based upon work supported by the U.S. Department of Energy, Office of Science, Office of Fusion Energy Sciences, using the DIII-D National Fusion Facility, a DOE Office of Science user facility, under Award(s) DE-FC02-04ER54698, DE-SC0021968, DE-SC0022270, and DE-SC0020298, DEAC02-09CH11466 (Princeton Plasma Physics Laboratory). Work also supported by the Chinese Academy of Sciences. This research was supported by R&D Program of 'KSTAR Experimental Collaboration and Fusion Plasma Research (EN2401-15)' through the Korea Institute of Fusion Energy (KFE) funded by Korea Ministry of Science and ICT (MIST). This work has been carried out within the framework of the EUROfusion Consortium, funded by the European Union via the Euratom Research and Training Programme (Grant Agreement No. 101052200—EUROfusion).

Disclaimer

ORCID iDs

C. Paz-Soldan https://orcid.org/0000-0001-5069-4934
S. Gu https://orcid.org/0000-0001-5159-939X
N. Leuthold https://orcid.org/0000-0002-5606-9782
P. Lunia https://orcid.org/0009-0004-4674-5275
P. Xie https://orcid.org/0000-0002-0567-646X
M.W. Kim https://orcid.org/0000-0002-8627-4584
S.K. Kim https://orcid.org/0000-0002-0701-8962
N.C. Logan https://orcid.org/0000-0002-3268-7359
J.-K. Park https://orcid.org/0000-0003-2419-8667
W. Suttrop https://orcid.org/0000-0003-0983-8881
Y. Sun https://orcid.org/0000-0002-9934-1328
D.B. Weisberg https://orcid.org/0000-0003-4510-0884
M. Willensdorfer https://orcid.org/0000-0002-1080-4200

References

[1] Zohm H. 1996 *Plasma Phys. Control. Fusion* **38** 105
[2] Leonard A.W. 2014 *Phys. Plasmas* **21** 090501
[3] Loarte A. *et al* 2003 *Plasma Phys. Control. Fusion* **45** 1549
[4] Federici G., Loarte A. and Strohmayer G. 2003 *Plasma Phys. Control. Fusion* **45** 1523
[5] Dux R., Janzer A. and Pütterich T. (ASDEX Upgrade Team) 2011 *Nucl. Fusion* **51** 053002
[6] Pitts R.A. *et al* 2013 *J. Nucl. Mater.* **438** S48
[7] Kallenbach A. *et al* (ASDEX Upgrade Team) 2005 *Plasma Phys. Control. Fusion* **47** B207
[8] Beurskens M.N.A. *et al* (JET-EFDA Contributors) 2014 *Nucl. Fusion* **54** 043001
[9] Kim H.-T., Sips A.C.C., Romanelli M., Challis C.D., Rimini F. G., Garzotti L., Lerche E., Buchanan J., Yuan X. and Kaye S. M. (JET contributors) 2018 *Nucl. Fusion* **58** 036020
[10] Loarte A. *et al* 2014 *Nucl. Fusion* **54** 033007
[11] Maingi R. 2014 *Nucl. Fusion* **54** 114016
[12] The ITPA PEP Experts 2024 Chapter 6: pedestal and edge physics of the special issue by the ITPA topical groups on progress toward burning plasma operation *Nucl. Fusion* submitted
[13] Evans T.E. 2015 *Plasma Phys. Control. Fusion* **57** 123001
[14] Waelbroeck F.L. 2009 *Nucl. Fusion* **49** 104025
[15] Nazikian R. *et al* 2015 *Phys. Rev. Lett.* **114** 105002
[16] Hu Q.M., Nazikian R., Grierson B.A., Logan N.C., Park J.-K., Paz-Soldan C. and Yu Q. 2019 *Phys. Plasmas* **26** 120702
[17] Fitzpatrick R. and Nelson A. 2020 *Phys. Plasmas* **27** 072501
[18] McKee G.R. *et al* 2013 *Nucl. Fusion* **53** 113011
[19] Lee J., Yun G.S., Choi M.J., Kwon J.-M., Jeon Y.-M., Lee W., Luhmann N.C. and Park H.K. 2016 *Phys. Rev. Lett.* **117** 075001
[20] Lee J. H., Jeon Y.M., In Y., Park G.Y., Yun G., Lee W., Kim M., Lee J.H., Ko W.H. and Park H.K. (The KSTAR Team) 2019 *Nucl. Fusion* **59** 066033
[21] Sung C. *et al* 2017 *Phys. Plasmas* **24** 112305
[22] Taimourzadeh S., Shi L., Lin Z., Nazikian R., Holod I. and Spong D. A. 2019 *Nucl. Fusion* **59** 046005
[23] Callen J.D., Cole A.J. and Hegna C.C. 2012 *Phys. Plasmas* **19** 112505

[24] Huijsmans G.T.A., Chang C.S., Ferraro N. M., Sugiyama L., Waelbroeck F. L., Xu X.Q., Loarte A. and Futatani S. 2015 *Phys. Plasmas* **22** 021805
[25] Bird T.M. and Hegna C.C. 2013 *Nucl. Fusion* **53** 013004
[26] Willensdorfer M. *et al* (The ASDEX Upgrade Team) 2017 *Phys. Rev. Lett.* **119** 085002
[27] Ryan D.A., Dunne M., Kirk A., Saarelma S., Suttrop W., Ham C. J., Liu Y.Q. and Willensdorfer M. (The ASDEX Upgrade Team and The MST1 Team) 2019 *Plasma Phys. Control. Fusion* **61** 095010
[28] Kim S.K. *et al* (JOREK Team) 2020 *Nucl. Fusion* **60** 026009
[29] Evans T. E. *et al* 2004 *Phys. Rev. Lett.* **92** 235003
[30] Moyer R.A. *et al* 2005 *Phys. Plasmas* **12** 056119
[31] Burrell K.H. *et al* 2005 *Phys. Plasmas* **12** 1
[32] Evans T.E. *et al* 2006 *Nat. Phys.* **2** 419
[33] Schaffer M.J., Menard J.E., Aldan M.P., Bialek J., Evans T.E. and Moyer R.A. 2008 *Nucl. Fusion* **48** 024004
[34] Becoulet M. *et al* 2008 *Nucl. Fusion* **48** 024003
[35] Sweeney R. M. *et al* 2020 *J. Plasma Phys.* **86** 865860507
[36] Kim H.K., Yang H.L., Kim G.H., Kim J.-Y., Jhang H., Bak J.S. and Lee G.S. 2009 *Fusion Eng. Des.* **84** 1029
[37] Jeon Y.M. *et al* (KSTAR team) 2012 *Phys. Rev. Lett.* **109** 035004
[38] Suttrop W. *et al* (The ASDEX Upgrade Team) 2009 *Fusion Eng. Des.* **84** 290
[39] Nazikian R. *et al* (The AUG, DIII-D and EUROfusion MST-1 Teams) 2016 *Proc. 26th IAEA Fusion Energy Conf.* (*Kyoto, Japan*, *October 2016*) p D/1–1 (available at: https://nucleus.iaea.org/sites/fusionportal/Shared Documents/FEC 2016/fec2016-preprints/preprint0952.pdf)
[40] Suttrop W. *et al* (The ASDEX Upgrade and MST1 Teams) 2018 *Nucl. Fusion* **58** 096031
[41] Sun Y., Liang Y., Qian J., Shen B. and Wan B. 2015 *Plasma Phys. Control. Fusion* **57** 045003
[42] Sun Y. *et al* 2016 *Phys. Rev. Lett.* **117** 115001
[43] Barlow I. *et al* 2001 *Fusion Eng. Des.* **58-59** 189
[44] Liang Y. *et al* 2007 *Phys. Rev. Lett.* **98** 265004
[45] Wolfe S.M. *et al* 2005 *Phys. Plasmas* **12** 056110
[46] Kirk A., Harrison J. R., Liu Y. Q., Nardon E., Chapman I.T. and Denner P. (The MAST team) 2012 *Phys. Rev. Lett.* **108** 255003
[47] Canik J.M. *et al* (The NSTX Team) 2010 *Phys. Rev. Lett.* **104** 045001
[48] Lawson J.D. 1957 *Proc. Phys. Soc.* B **70** 6
[49] Oyama N. *et al* (The ITPA Pedestal Topical Group) 2006 *Plasma Phys. Control. Fusion* **48** A171
[50] Viezzer E. 2018 *Nucl. Fusion* **58** 115002
[51] Paz-Soldan C. (The DIII-D Team) 2021 *Plasma Phys. Control. Fusion* **63** 083001
[52] Hubbard A.E. *et al* (The Alcator C-Mod, ASDEX Upgrade and DIII-D Teams) 2016 *Nucl. Fusion* **56** 086003
[53] Kim M. *et al* 2020 *Phys. Plasmas* **27** 112501
[54] Thomsen K. (The H-mode Database Working Group) 2002 *Fusion Eng. Des.* **60** 347
[55] Evans T. E. 2008 *Chaos, Complexity and Transport* (World Scientific) pp 147–76
[56] Hu Q. M., Nazikian R., Grierson B. A., Logan N. C., Orlov D. M., Paz-Soldan C. and Yu Q. 2020 *Phys. Rev. Lett.* **125** 045001
[57] Angioni C., Sertoli M., Bilato R., Bobkov V., Loarte A., Ochoukov R., Odstrcil T., Pütterich T. and Stober J. (The ASDEX Upgrade Team) 2017 *Nucl. Fusion* **57** 056015
[58] In Y. *et al* (The 3D Physics Task Force in KSTAR) 2019 *Nucl. Fusion* **59** 056009
[59] Neumeyer C. *et al* 2011 *Fusion Sci. Technol.* **60** 95
[60] Daly E.F. *et al* 2013 *Fusion Sci. Technol.* **64** 168
[61] Matsunaga G., Takechi M., Sakurai S., Suzuki Y., Ide S. and Urano H. 2015 *Fusion Eng. Des.* **98–99** 1113
[62] Yoshida M. *et al* 2022 *Plasma Phys. Control. Fusion* **64** 054004
[63] Paz-Soldan C., Eidietis N.W., Liu Y.Q., Shiraki D., Boozer A.H., Hollmann E.M., Kim C.C. and Lvovskiy A. 2019 *Plasma Phys. Control. Fusion* **61** 054001
[64] Jeon Y. M., In Y., Park J.-K., Kim J. H., Park G. Y., Han H. S., Yoon S. W., Oh Y. K. and Ahn J. W. 2018 *Proc. 27th IAEA Fusion Energy Conf.* (*Ahmedabad, India, October 2018*) p EX/7 (available at: https://nucleus.iaea.org/sites/fusionportal/Shared Documents/FEC 2018/fec2018-preprints/preprint0750.pdf)
[65] Gu S. *et al* (The ASDEX Upgrade and The EUROfusion MST1 Teams) 2022 *Nucl. Fusion* **62** 076031
[66] Gu S. 2023 Private Communication
[67] Wade M.R. *et al* 2015 *Nucl. Fusion* **55** 023002
[68] Kim J., Park G. Y., Bae C., Yoon S., Han H., Yoo M.-G., Park Y.-S., Ko W.-H., Juhn J.-W. and Na Y.S. (The KSTAR Team) 2017 *Nucl. Fusion* **57** 022001
[69] Lanctot M.J. *et al* (The DIII-D Team) 2013 *Nucl. Fusion* **53** 083019
[70] Gu S. *et al* 2019 *Nucl. Fusion* **59** 026012
[71] Chen R., Lyons B.C., Weisberg D., Lao L.L., Ding S., Sun Y., Garofalo A.M., Gong X. and Xu G. 2022 *Nucl. Fusion* **62** 036022
[72] Park J.-K. *et al* 2018 *Nat. Phys.* **14** 1223
[73] Yang S.M. *et al* 2020 *Nucl. Fusion* **60** 096023
[74] Paz-Soldan C. *et al* 2015 *Phys. Rev. Lett.* **114** 105001
[75] Park J.-K. and Logan N.C. 2017 *Phys. Plasmas* **24** 032505
[76] Zhou L., Liu Y. Q., Wenninger R., Wang S. and Yang X. 2018 *Nucl. Fusion* **58** 076025
[77] Ryan D.A., Liu Y.Q., Kirk A., Suttrop W., Dudson B., Dunne M. and Willensdorfer M. (The ASDEX Upgrade Team and The EUROfusion MST1 Team) 2018 *Plasma Phys. Control. Fusion* **60** 065005
[78] Logan N.C., Zhu C., Park J.-K., Yang S.M. and Hu Q. M. 2021 *Nucl. Fusion* **61** 076010
[79] Evans T.E. *et al* 2005 *Nucl. Fusion* **45** 595
[80] Evans T.E. *et al* 2008 *Nucl. Fusion* **48** 10
[81] Hu Q.M. *et al* 2021 *Phys. Plasmas* **28** 052505
[82] Fitzpatrick R., Kim S.-K. and Lee J. H. 2021 *Phys. Plasmas* **28** 082511
[83] Snyder P.B., Osborne T.H., Burrell K.H., Groebner R.J., Leonard A.W., Nazikian R., Orlov D.M., Schmitz O., Wade M.R. and Wilson H.R. 2012 *Phys. Plasmas* **19** 056115
[84] Fenstermacher M.E. *et al* (The DIII-D Team) 2008 *Phys. Plasmas* **15** 056122
[85] Suttrop W. *et al* (ASDEX Upgrade Team) 2011 *Phys. Rev. Lett.* **106** 225004
[86] Sun Y. 2023 *Proc. 29th IAEA Fusion Energy Conf.* (*London, UK, October 2023*)
[87] Xie P. *et al* (The EAST Team) 2023 *Nucl. Fusion* **63** 096025
[88] Wagner F. *et al* 2010 *Plasma Phys. Control. Fusion* **52** 124044
[89] Kirk A. *et al* (MAST and ASDEX Upgrade Teams) 2015 *Nucl. Fusion* **55** 043011
[90] Sauter O., Angioni C. and Lin-Liu Y.R. 1999 *Phys. Plasmas* **6** 2834
[91] Martin Y. R. and Takizuka T. (The ITPA CDBM H-mode Threshold Database Working Group) 2008 *J. Phys.: Conf. Ser.* **123** 012033
[92] Ryter F., Barrera Orte L., Kurzan B., McDermott R.M., Tardini G., Viezzer E., Bernert M. and Fischer R. (The ASDEX Upgrade Team) 2014 *Nucl. Fusion* **54** 083003
[93] Loarte A. *et al* 2021 *Nucl. Fusion* **61** 076012
[94] Petty C.C., Wade M.R., Kinsey J.E., Groebner R.J., Luce T.C. and Staebler G.M. 1999 *Phys. Rev. Lett.* **83** 3661
[95] Prater R. 2004 *Phys. Plasmas* **11** 2349

[96] Kaye S.M., Gerhardt S. P., Guttenfelder W., Maingi R., Bell R.E., Diallo A., Leblanc B.P. and Podesta M. 2013 *Nucl. Fusion* **53** 063005

[97] Howard N.T., Holland C., White A.E., Greenwald M. and Candy J. 2016 *Nucl. Fusion* **56** 014004

[98] Angioni C., Bilato R., Casson F., Fable E., Mantica P., Odstrcil T. and Valisa M. (ASDEX Upgrade Team and JET Contributors) 2017 *Nucl. Fusion* **57** 022009

[99] Grierson B.A., Staebler G.M., Solomon W.M., McKee G.R., Holland C., Austin M. E., Marinoni A., Schmitz L. and Pinsker R.I. (DIII-D Team) 2018 *Phys. Plasmas* **25** 022509

[100] Lee S.G. 2020 *Phys. Plasmas* **27** 064503

[101] Troyon F., Gruber R., Saurenmann H., Semenzato S. and Succi S. 1984 *Plasma Phys. Control. Fusion* **26** 209

[102] Yushmanov P.N., Takizuka T., Riedel K.S., Kardaun O., Cordey J.G., Kaye S.M. and Post D.E. 1990 *Nucl. Fusion* **30** 1999

[103] Kim M. *et al* 2023 *Nucl. Fusion* **63** 086032

[104] Doyle E. J. *et al* (ITPA Transport Physics Topical Group, ITPA Confinement Database and Modelling Topical Group and ITPA Pedestal and Edge Topical Group) 2007 *Nucl. Fusion* **47** S18

[105] Heidbrink W.W. and Sadler G.J. 1994 *Nucl. Fusion* **34** 535

[106] Pankin A., McCune D., Andre R., Bateman G. and Kritz A. 2004 *Comput. Phys. Commun.* **159** 157

[107] Kim H. 2023 *Nucl. Fusion* **64** 016033

[108] Na Y.-S. *et al* (KSTAR team) 2020 *Nucl. Fusion* **60** 086006

[109] Laggner F.M. *et al* (The DIII-D Team) 2020 *Nucl. Fusion* **60** 076004

[110] Wurzel S.E. and Hsu S.C. 2022 *Phys. Plasmas* **29** 062103

[111] Snyder P.B. *et al* 2019 *Nucl. Fusion* **59** 086017

[112] Lehnen M. *et al* 2015 *J. Nucl. Mater.* **463** 39

[113] ITER Physics Expert Group on Confinement and Transport, ITER Physics Expert Group on Confinement Modelling and Database and ITER Physics Basis Editors 1999 *Nucl. Fusion* **39** 2175

[114] Verdoolaege G., Kaye S., Angioni C., Kardaun O., Maslov M., Romanelli M., Ryter F. and Thomsen K. (The ASDEX Upgrade Team, The EUROfusion MST1 Team and JET Contributors) 2021 *Nucl. Fusion* **61** 076006

[115] Logan N.C. *et al* 2020 *Plasma Phys. Control. Fusion* **62** 084001

[116] Aymar R., Chuyanov V.A., Huguet M., Shimomura Y., (ITER Joint Central Team and ITER Home Teams) 2001 *Nucl. Fusion* **41** 1301

[117] Creely A.J. *et al* (The SPARC Team) 2020 *J. Plasma Phys.* **86** 865860502

[118] Chrystal C., Grierson B.A., Haskey S.R., Sontag A.C., Poli F.M., Shafer M.W. and Degrassie J.S. 2020 *Nucl. Fusion* **60** 036003

[119] Rodriguez-Fernandez P., Howard N.T., Greenwald M., Creely A.J., Hughes J.W., Wright J.C., Holland C., Lin Y. and Sciortino F. (The SPARC team) 2020 *J. Plasma Phys.* **86** 865860503

[120] Eich T. *et al* (ASDEX Upgrade Team and JET EFDA Contributors) 2013 *Nucl. Fusion* **53** 093031

[121] Petrie T. *et al* 2011 *Nucl. Fusion* **51** 073003

[122] Jia M. *et al* 2021 *Nucl. Fusion* **61** 106023

[123] Sun Y. *et al* (EAST Contributors) 2021 *Nucl. Fusion* **61** 106037

[124] Shin H., Hwang J., Han Y., Shin G., Lee H., Chai K.-B. and Choe W. 2023 *Nucl. Fusion* **63** 044003

[125] Burrell K.H. 1997 *Phys. Plasmas* **4** 1499

[126] Burrell K.H. 2020 *Phys. Plasmas* **27** 060501

[127] Kotschenreuther M., Dorland W., Beer M.A. and Hammett G.W. 1995 *Phys. Plasmas* **2** 2381

[128] Keilhacker M. *et al* (JET Team) 1999 *Nucl. Fusion* **39** 209

[129] Ishida S., Barabaschi P. and Kamada Y. (The JT-60SA Team) 2011 *Nucl. Fusion* **51** 094018

[130] Logan N., Sweeney R. M., Markovic T., Paz-Soldan C., Park J.-K., Yang S. M., Hu Q. M. and Zhu C. 2021 *Bull. Am. Phys. Soc.* **2021** JO07.004

[131] Vondracek P. *et al* 2021 *Fusion Eng. Des.* **169** 112490